RSC Applied Interfaces

ROYAL SOCIETY OF CHEMISTRY

PAPER

View Article Online
View Journal | View Issue

Check for updates

Cite this: *RSC Appl. Interfaces*, 2025, **2**, 741

In situ thermal solvent-free synthesis of doped ZIF-8 as a highly efficient visible-light-driven photocatalyst†

Farah Naz,[ab] Chun Hong Mak,[ab] Zhe Wang,[ab] Haihang Tong,[ab] Shella Permatasari Santoso,*[c] Minshu Du,[d] Ji-Jung Kai,[e] Kuan-Chen Cheng,[fghij] Chang-Wei Hsieh,[klo] Wenxin Niu,[m] Zheng Hu[n] and Hsien-Yi Hsu*[ab]

Received 11th December 2024,
Accepted 14th January 2025

DOI: 10.1039/d4lf00410h

rsc.li/RSCApplInter

Developing an economical and effective catalyst to remove organic pollutants from wastewater remains a significant challenge to maintaining a healthy, green environment. The metal–organic frameworks (MOFs) have drawn considerable attention to renewable energy and environmental remediation due to their porous crystalline structure. In this context, we develop a straightforward, environmentally friendly, solvent-free, *in situ* thermal (IST) method to synthesize doped zeolitic imidazole frameworks (ZIF-8). The solvent-free IST technique surpasses the traditional synthesis procedures in efficiency due to a single-step and solvent-free process with a short processing time and a low precursor ratio. Notably, doped ZIF-8 photocatalysts against concentrated methylene blue (MB) and rhodamine B (RhB) degradation exhibit superior photocatalytic performance under visible light exposure. An in-depth study of the effect of dye concentration and pH on doped ZIF-8 is also performed. The kinetic study *via* photocatalytic isotherms confirms that the photodegradation mechanism follows the pseudo-first-order kinetic model. Following active species trapping experiments, we confirm that the hydroxyl radicals play a substantial role in MB degradation with optimized Fe@ZIF-8. Moreover, the Fe@ZIF-8 does not significantly lose its photocatalytic activity for degrading MB after three cycles, indicating its enduring reusability and stability. Thus, this study provides a novel approach to developing the doped MOF as a photocatalyst with enhanced photocatalytic activity for wastewater treatment.

1. Introduction

Water is an indispensable element that sustains all organisms on our planet. In the past few years, we have witnessed a consistent rise in population, an increase in the worldwide economy, and our reliance on conventional fossil fuels, giving rise to water pollution.[1] The above-mentioned issues arose simultaneously with the shortage of water resources; therefore, the main task of the scientific community is to remove water pollutants. Such strategies require the development of more advanced technologies or adapting presently used materials or technology.[2] The detrimental

[a] *School of Energy and Environment, Department of Materials Science and Engineering, Centre for Functional Photonics (CFP), City University of Hong Kong, Kowloon Tong, Hong Kong, China. E-mail: sam.hyhsu@cityu.edu.hk*
[b] *Shenzhen Research Institute of City University of Hong Kong, Shenzhen, 518057, China*
[c] *Department of Chemical Engineering, Faculty of Engineering, Widya Mandala Surabaya Catholic University, Kalijudan No. 37, Surabaya 60114, East Java, Indonesia. E-mail: shella@ukwms.ac.id*
[d] *School of Materials Science and Engineering, Northwestern Polytechnical University, Xi'an, Shaanxi 710072, China*
[e] *Department of Mechanical Engineering, City University of Hong Kong, Kowloon Tong, Hong Kong, China*
[f] *Institute of Biotechnology, National Taiwan University, No. 1, Sec. 4, Roosevelt Rd., Taipei 10617, Taiwan*
[g] *Department of Optometry, Asia University, 500, Lioufeng Rd., Wufeng, Taichung, Taiwan*
[h] *Department of Medical Research, China Medical University Hospital, China Medical University, 91, Hsueh-Shih Road, Taichung, Taiwan*
[i] *Institute of Food Science and Technology, National Taiwan University, No. 1, Sec. 4, Roosevelt Rd., Taipei 10617, Taiwan*
[j] *Dept of Food Science, Fu Jen Catholic University, 24205, New Taipei City, Taiwan*
[k] *Department of Food Science and Biotechnology, National Chung Hsing University, 145 Xingda Rd., South Dist., Taichung City, Taiwan*
[l] *Department of Food Science, National Ilan University, Shennong Road, Yilan City 26047, Taiwan*
[m] *State Key Laboratory of Electroanalytical Chemistry, Changchun Institute of Applied Chemistry, Chinese Academy of Sciences, 5625 Renmin Street, Changchun, Jilin 130022, P. R. China*
[n] *Key Laboratory of Mesoscopic Chemistry of MOE and Jiangsu Provincial Laboratory for Nanotechnology, School of Chemistry and Chemical Engineering, Nanjing University, Nanjing 210023, China*
[o] *Department of Medical Research, China Medical University Hospital, Taichung City, Taiwan*

† Electronic supplementary information (ESI) available. See DOI: **https://doi.org/10.1039/d4lf00410h**

effects of dye effluent on the environment have been widely noticed, including aesthetic contamination, toxicity, and impact on aquatic life.[3] Furthermore, mainly textile dyes provide long-lasting color and are non-biodegradable. The majority of colors are also challenging to remove from the wastewater.[2e] A limited variety of water treatment technologies, including chemical, physical, and biological approaches, have succeeded in dye removal from effluent.[4] Adsorption of activated carbon to remove organic contaminants is one of the most effective color removal processes; nevertheless, the issue of its high cost remains. Despite oxidation by ozonation and hypochlorite being an effective decolorization method, there are more efficient methods for dye removal due to the high cost of apparatus, operation, and secondary pollution.[5] As a result, improving advanced processing technology to remove dyes from wastewater is an essential environmental preservation.

Based on the ongoing research and development of technologies for environmental protection, advanced oxidation processes (AOPs) are considered a possible way to solve the abovementioned ecological problems.[4d,6] Among AOP technologies, photocatalysis has drawn attention to energy conservation and environmental remediation (*e.g.*, organic dye degradation), solar energy conversion, and organic photosynthesis due to its ease of use, low selectivity, and moderate reaction conditions. Thus, the photocatalytic approach is a cost-effective, versatile, and efficient water treatment method.[6a,f]

Photocatalytic technology has advanced tremendously since Fujishima and Honda *et al.* discovered in 1972 that single titanium dioxide (TiO_2) crystals can catalyze water hydrolysis to produce hydrogen when exposed to ultraviolet light.[7] Photocatalytic oxidation technologies have grown fast and recently become increasingly important in the water treatment industries. Several semiconductor photocatalysts are introduced to remove organic pollutants from wastewater, *e.g.* TiO_2,[8] Fe_2O_3,[9] ZnO,[10] MoS_2,[11] g-C_3N_4,[12] CdS, *etc.*[13] The technology of green photocatalysis has effectively eliminated hazardous effluents in industrial wastewater. However, some problems still need to be addressed, such as inadequate mineralization, inefficient charge transfer efficiency, and restricted solar energy usage.[14] To completely mineralize organic effluents, photocatalysts must efficiently separate charges and maximize light absorption while retaining oxidation capability. Nonetheless, the broader bandgap of these systems as photocatalysts may substantially restrict their efficiency.[15] A practical and straightforward method is to combine materials with narrow band gaps to increase the efficiency of photocatalysis by facilitating electron transport and reducing the rate of electron–hole recombination.

It is essential to find photocatalytic materials that are durable and affordable to replace traditional ones. Metal–organic frameworks (MOFs) are crystalline materials with metals or metal clusters connecting nodes and polyfunctional molecular building blocks having high specific surface area and well-organized structures that have drawn significant interest in various domains. These fields include gas storage,[16] gas separation,[17] drug delivery,[18] chemical sensors,[19] heterogeneous catalyst[20] and photocatalyst.[2e,15a,21] Compared to other metal–organic frameworks (MOFs), ZIF-8, primarily made of imidazolate organic ligand and Zn^{2+} center ions, displays exceptional chemical and thermal stability.[22] The more specific surface area and uniform distribution of active sites in ZIF-8 make it a desirable candidate for functionalization to increase its efficiency as a photocatalysis.[23]

As a class of MOFs, ZIFs are topologically isomorphic with zeolites. ZIFs and MOFs can be prepared using different synthesis methods for various applications. In the conventional method for preparing ZIFs and MOFs, the precursor ligand and metal ion are typically dispersed in organic solvents before heating under specific conditions. The procedure may be executed for an extended duration, ranging from several hours to one week. In synthesizing ZIFs and MOFs, organic solvents such as dimethylformamide (DMF), tetrahydrofuran (THF), or alcohol are frequently utilized due to their significant ability to solubilize precursors and facilitate crystal formation. An environmentally sustainable approach was discovered at ambient temperature, employing water as the solvent to make nanocrystal products with a significantly higher yield than solvothermal synthesis.[24] However, only a few precursors, including metals and ligands, show water solubility, leading to a shortage of successes in synthesizing ZIFs and MOFs. The green approach was then improved by advances in synthesis methods, including spray drying, microwave, electrochemistry, mechanochemical, *etc.*[25] A microwave-assisted method for the rapid crystallization of MOFs has been developed. However, a particular instrument characterized by a sophisticated operation is needed. Unconventional nucleation agent inoculation and electrochemical deposition techniques have produced ZIFs. In comparison to previously reported methods, several drawbacks to the utilization of contemporary methods remain, *e.g.*, high energy demands, procurement of cost or hazardous precursors and organic solvents, lengthened reaction durations, surplus ligand (ligand/metal > 1), use of additives (acid/base), and dependence on sophisticated instruments. The traditional process results in a non-environmentally friendly materials synthesis due to the different wastes generated throughout the synthesis and post-treatment processes. In terms of utilizing MOF and ZIF materials for practical applications, undergoing extra post-treatments, such as purification or activation of solvent, salt residue, or side product, is imperative. Accordingly, ZIF production and exploitation for diverse applications are restricted for the aforementioned reasons. Furthermore, industrialization is still a significant problem in the large-scale synthesis of ZIFs and MOFs.[26] Therefore, for ZIFs and MOFs applied in the real market, developing a new synthetic strategy with an environmentally friendly and facile approach is essential and challenging.

This study presents a practical approach for synthesizing doped ZIF-8, utilizing a simple and direct one-pot synthesis procedure, specifically called an *in situ* thermal treatment (IST) method. Noticeably, the ZIFs prepared using this technique have yet to be reported for use in photocatalytic wastewater treatment. This method can quickly produce highly porous crystalline materials without adding additives or solvents. After comparing as-synthesized materials with traditionally synthesized ZIFs, it is noticed that the prepared materials are isostructural and possess the same properties in terms of surface area, porosity, and thermal stability. It is worth noting that the produced materials do not require any posttreatment or activation procedure. The ZIFs produced by this efficient, cost-effective IST method ultimately perform enhanced chemical and physical properties. Metal nanoparticles, such as Fe and Ni, have gained significant attention as co-catalysts compared with other material options due to their ability to efficiently separate charges through the formation of Schottky barriers at the heterogeneous nanoscale junctions and surface plasmon resonance (SPR), thereby significantly improving the photocatalytic performance.[15a,27] The catalytic activity of the as-prepared materials has been determined by the photocatalytic degradation of dyes in wastewater treatment. We confirm doped ZIF-8 exhibits superior performance compared with ZIF-8, potentially making a significant contribution to real-world uses in wastewater treatment. Consequently, ZIF-8 prepared using the IST method instead of traditional synthesis processes opens up an avenue for metal–organic frameworks for commercializing photocatalytic energy and environmental applications.

2. Materials and methods

2.1. Materials

The chemicals used in this work were bought from commercial suppliers and utilized without going through any purification processes. Aladdin supplied zinc acetylacetonate hydrate (97%), 2-methylimidazole (2-MIM, 98%), iron acetylacetonate (98%), and nickel acetylacetonate (97%), benzoquinone (97%) and ammonium oxalate (98), which were utilized as initially received. MACKLIN and Aladdin supplied Methylene Blue (MB, 98%) and rhodamine B (RhB, 99%). Duksan Pure Chemicals, Korea, provided hydrochloric acid (HCL, 37%) and sodium hydroxide (NaOH, 99.9%). Anaqua Global International Inc. limited supplied *N*,*N*-dimethylformamide (DMF, 99.8%), isopropyl alcohol (IPA, 99.8%), and methanol (MeOH, 99.8%). Merck's Milli-Q® Direct Water Purification System provides deionized (DI) water.

2.2. Preparation of ZIF-8

First, the Zn(II) acetylacetonate (0.959 mmol, 263 mg) and 2-methylimidazole (3.99 mmol, 328 mg) were combined and mashed in a mortar for almost five minutes in an ambient atmosphere to synthesize ZIF-8. After that, the resulting solid mixtures were put in an alumina boat ($30 \times 60 \times 15$ mm^3) and then moved inside the muffle furnace (TL 1200, Nanjing Bo Yun Tong Instrument Technology Co. Ltd) into a quartz tube (O.D.: 60 mm, length: 1000 mm). An Ar or N_2 (100 cm^3 min^{-1}) stream was flown in the system. Two steps were employed to set the temperature program: a 30-minute rise from room temperature to 100 °C, then raised to 200 °C (5 °C min^{-1}) and maintained constant for one hour. After cooling, the final product was collected and employed for further characterization and applications. The product's yield was calculated using the eqn (1).

$$\text{Synthesis yield (\%)} = \frac{\text{average weight of the product}}{\text{theoretical product}} \times 100 \quad (1)$$

2.3. Preparation of M@ZIF-8

In a typical synthesis of M@ZIF-8, the as-prepared ZIF-8 (300 mg), 2-methylimidazole (0.84 mmol, 69 mg), and Fe(III) acetylacetonate (0.11 mmol, 37.2 mg) were mixed and ground in a mortar for about 5 minutes under an ambient atmosphere to produce Fe@ZIF-8. Ni@ZIF-8 was prepared in the same way as Fe@ZIF-8, with Ni(II) acetylacetonate (0.11 mmol, 27 mg) replacing Fe(III) acetylacetonate. Fe@ZIF-8 and Ni@ZIF-8 used the same product mixing, synthesis, temperature program, time, and recovery procedures that ZIF-8 did.

2.4. Characterization

The crystalline phases of the ZIF-8 and doped ZIF-8 as-made photocatalyst were examined using a PANalytical X'Pert3 X-ray diffractometer in the 2theta range of 5–90 degrees at a tension of 40 kV and 40 mA current under Cu-Kα radiation (λ = 1.54 Å). The morphology was confirmed by transmission electron microscopy (TEM, American, FEI Talos F200X G2), scanning electron microscopy (ZEISS EVO MA10 SEM at 15 kV), and field-emission scanning electron microscopy (FESEM; Hitachi, SU-8010, 10 kV, working distance: 6.8 mm). Surface electronic valence states were analyzed utilizing a Thermo Scientific apparatus (ESCALAB220i-XL) and a monochromatic Al Kα X-ray source (1486.68 eV). The carbon 1s peak at 284.6 eV was used to calibrate the binding energy. Thermogravimetric analyses (TGA) were performed using TA SDT650 equipment with a 20 °C min^{-1} heating rate in a nitrogen atmosphere. The ATR-FTIR (attenuated total reflectance-Fourier transform infrared spectroscopy) analysis was studied using an IRaffinity-1 (Shimadzu Corporation, Japan) spectrometer equipped with a PIKE MIRacle ATR module to observe the functional group of synthesized samples. All samples were recorded in the 400–4500 cm^{-1} range with 50 scans and 4 cm^{-1} resolution. Raman spectra were collected using Renishaw's inVia Raman microscopy. Under 99.999% pure N_2, the adsorption–desorption was measured using an ASAP 2020 Analyzer (Micrometrics Instruments).

Furthermore, materials were activated for three hours at 200 °C under a dynamic vacuum before the adsorption measurement. The Langmuir and Brunauer–Emmett–Teller (BET) analysis was employed to study the surface area and porosity of the prepared material. The fitting range for the linearized BET and Langmuir equations was $0.003 < P/P_0 < 0.05$. Nitrogen (N_2) was used in a constant volume adsorption/desorption device (Autosorb iQ Station 1) to study the surface properties. To prevent moisture, the prepared materials were degassed at 200 °C for approximately two hours before the Brunauer–Emmett–Teller (BET) method (surface-area nova-touch device) was used to analyze the surface area at −196 °C. MB and RhB's ultraviolet-visible diffused reflectance spectroscopy (UV-vis DRS) spectra were measured *via* a UV-vis spectrophotometer (PerkinElmer, lambda 1050+) before and after the photodegradation. The Kubelka–Munk theory was used to draw Tauc plots from these spectra.

2.5. Photocatalytic activity measurements

The photocatalytic performance of the prepared materials was studied by utilizing MB and RhB degradation. The photocatalysis studies were carried out in the photoreactor under ambient circumstances. Photocatalytic studies were carried out using a PLS-SXE300E high-power xenon light source with a cut-off filter of 420 nm, which produces visible light. For each photodegradation test, photocatalyst (10 mg) was added to a 25 mL aqueous solution of MB and RhB (10 and 20 mg L^{-1}, respectively). Before the visible light illuminations, the sample solutions were stirred under the dark for 30 minutes to achieve adsorption–desorption stability. After 30 minutes, the sample solution was transported to a reactor, which started the photodegradation reaction. The visible light was exposed to the as-prepared solution for a set time. After the allotted time, 5 mL of solution was removed from the bulk sample solution. The solution underwent filtering through a hydrophobic syringes filtration (Sartorius, PTFE, 0.2 μm pore-size) to remove solid particles and obtain the translucent dye liquid. The degradation of MB and RhB in the solutions was measured using a UV-visible spectrophotometer, and the degradation rate was estimated using the equation below.

$$\eta\% = \frac{C_0 - C_t}{C_0} \times 100 \quad (2)$$

The photocatalytic degradation rate is denoted by η, C_0 represents the initial concentrations, and C_t represents the final concentration at time t. The MB's and RhB's most noteworthy absorption peaks were 664 nm and 556 nm, respectively. Furthermore, the pH and dye concentrations were studied. To adjust the pH, HCl and NaOH were added to the solution. HCl and NaOH were added to the dye solutions. For the recycling investigation, the photocatalyst was pulled out from the photoreactor after every run, and a 5 mL sample was taken, washed, and dried before the photocatalytic tests were performed using comparable techniques.

3. Results and discussion

3.1. Material characterizations

ZIFs based on the 2-methylimidazole linker have been widely synthesized and used in various applications.[26g,28] ZIF-8 and doped ZIFs, in particular, exhibit exceptional properties and performance in various applications, comprising molecular separation, gas adsorption, electrochemistry, catalysis, and so on.[29] This study adopts the *in situ* thermal (IST) strategy to develop ZIF-8 and doped ZIF-8. To synthesize ZIF-8, mixtures of 2-methylimidazole and Zn(II) acetylacetonate were heated up in a tube-shaped furnace under an inert atmosphere (Ar or N_2). Then, ZIF-8 reacted with Fe(III) acetylacetonate and Ni(II) acetylacetonate to synthesize Fe and Ni-doped ZIF-8, respectively.

ZIFs are known for their outstanding properties among MOFs, notably because of porosity, high crystallinity, thermal stability, and surface area. The solid crystalline products prepared *via* thermal treatment are characterized using powder X-ray diffraction (XRD), as illustrated in Fig. 1a. The XRD patterns of the as-prepared sample demonstrate the crystal transformation after the IST treatment at 200 °C. The diffraction patterns of the prepared materials are observed within the range of 5 to 55°. The 2θ values corresponding to these patterns are found to be 7.09, 10.05, 12.49, 14.44, 16.24, and 17.79°, which are assigned to the lattice planes 110, 200, 211, 220, 310, and 222, respectively. As previously reported,[15a] the presence of well-defined peaks in the ZIF-8 material suggests a high level of crystallinity. The crystalline pattern was also studied for Fe and Ni-doped ZIF-8 materials, as depicted in Fig. 1a. The crystalline pattern of the materials doped with Fe and Ni in ZIF-8 exhibits a remarkable similarity to that observed in pure ZIF-8. The dispersion of iron (Fe) and nickel (Ni) particles within ZIF-8 crystals results in a slight improvement in crystallinity. This finding confirms that the prepared catalysts possess the sodalite-type topology (SOD), as reported previously,[30] proving the pure crystal phase of prepared materials. Furthermore, it is noteworthy that no impurity or supplementary peak was detected in any of the spectra analyzed after Fe or Ni doping.

ZIF's excellent thermal stability is one of its most significant benefits over other MOFs. The thermal gravimetric analysis (TGA) was used to check the thermal stability and impurities of synthesized ZIF-8 and doped ZIF-8. The percentage weight change or mass change of the synthesized samples is observed in terms of temperature. It is worth mentioning that the as-prepared ZIFs using the IST method were assessed *via* TGA without any pre-treatment or post-activation (Fig. 1b). The TGA results reveal that thermal activities occurred up to 550 °C shortly after degradation (21.803% weight change at 656.78 °C), as shown in the TGA profile of ZIF-8 (Fig. 1b). At 500 °C, a slight weight change can be attributed to inadequate coordination or a structural

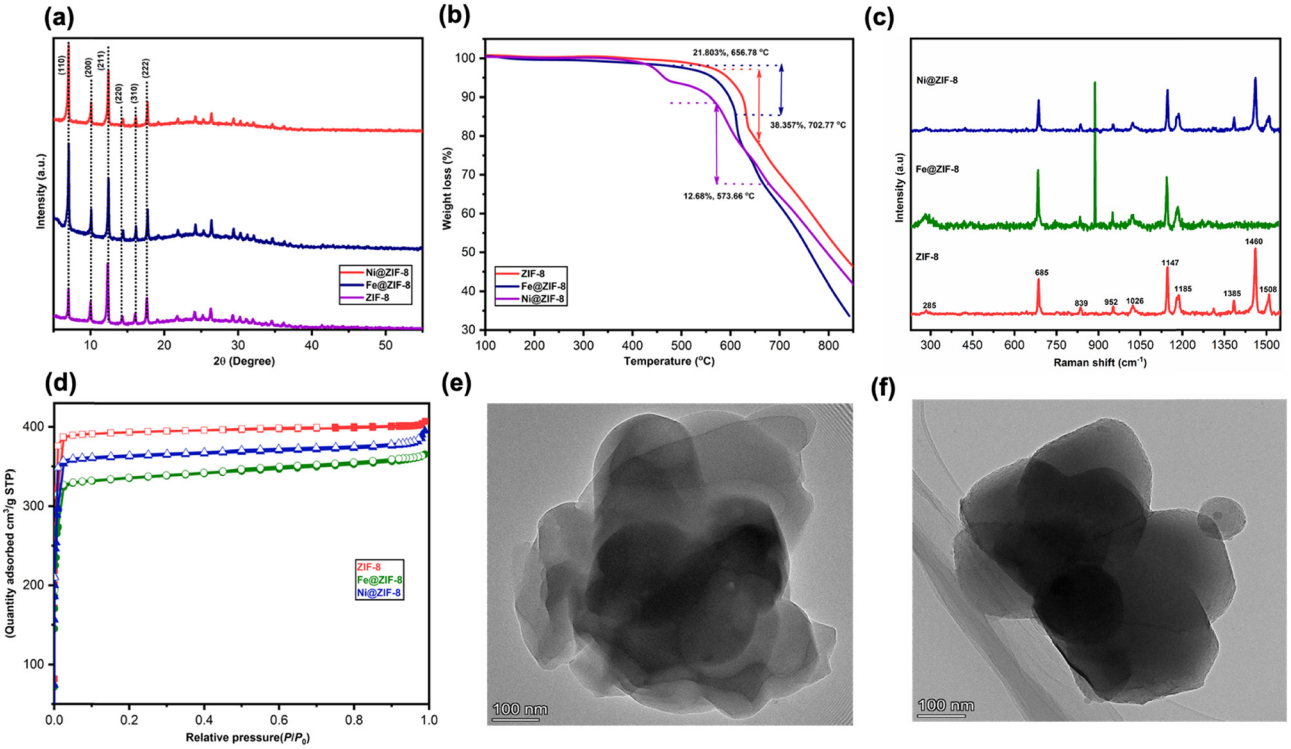

Fig. 1 (a) X-ray diffraction pattern (XRD), (b) the thermo-gravimetric analysis (TGA), (c) Raman spectrum, and (d) N_2 adsorption–desorption isotherms of ZIF-8, Fe@ZIF-8, and Ni@ZIF-8. Transmission electron microscopy (TEM) of (e) Fe@ZIF-8 and (f) Ni@ZIF-8.

flaw as that temperature exceeds the 2-MIM boiling point.[26g] TGA study revealed that ZIF-8 is thermally stable up to 500 °C. Concerning doped ZIFs, Fe@ZIF-8 shows a stable crystal structure up to 500 °C, the same as ZIF-8. After that, 38.35% weight loss is observed at 702.77 °C. The TGA of Ni@ZIF-8 shows good stability until 450 °C; (a) after that, the materials gradually degrade with the increment in temperature (12.68% weight loss occurs at 573.66 °C). The initial weight loss of 1–3% is noticed for ZIF-8 and Fe@ZIF-8, while 7% weight loss is observed for Ni@ZIF-8 until 500 °C. The ZIF-8 material under analysis deteriorates progressively as the temperature rises, ultimately transforming into carbon and zinc species. At the same time, in the case of doped Fe and Ni ZIF-8, there are carbon, zinc, nickel, and iron species (>700 °C). The materials have no precursor residuals, by-products, or guest molecules, as evidenced by the absence of a discernible weight shift at temperatures below 500 °C. Also, moisture desorption from the material pores and surfaces is missing and does not contribute to deterioration.[31] The ZIF-8 and doped ZIF-8 prepared using the IST method shows higher thermal stability than the ZIF-8 or Fe and Ni-doped ZIF-8 synthesized through the traditional methods.[2e,22] The decrease in weight seen at 500 °C in all produced materials is attributed to structural deterioration and deterioration of organic ligands. This indicates that all catalysts exhibit excellent thermal stability, with a collapse temperature of 500 °C for ZIF-8 and Fe@ZIF-8 and 400 °C for Ni@ZIF-8.

The structural identification of the ZIF-8 and Fe and Ni-doped ZIF-8 material was also investigated using Raman spectroscopy (Fig. 1c). The developed samples' spectra exhibit different peaks correlating with the molecule's stretching, bending, out-of-plane, aromatic, and asymmetric bands. The Zn–N stretching responsible for the characteristic Raman shift of ZIF-8 is observed at 285 cm^{-1}. The C–H out-of-plane bend bands are 839 cm^{-1}, 952 cm^{-1}, and 1026 cm^{-1}. The band viewed at 685 cm^{-1} is attributed to the puckering of the imidazole ring. The 1147 cm^{-1} and 1185 cm^{-1} bands are assigned to C_5–N and C–N stretching, respectively. The 1385 cm^{-1}, 1460 cm^{-1}, and 1508 cm^{-1} bands are associated with the bending CH_3, C–H wag, and stretching C–C, respectively. The Raman spectra of Ni@ZIF-8 strongly reflect a similar bond of ZIF-8. Ni@ZIF-8 shows a small shift, indicating that the bond length of ZIF molecules has increased. The Raman spectra of Fe@ZIF-8 show identical peaks as ZIF-8 and Ni@ZIF-8. Bands at 1385 cm^{-1}, 1460 cm^{-1}, and 1508 cm^{-1} are absent in the case of F_2@ZIF-8, possibly due to their molecular, crystal structure, and fluorescence interference from the sample.[32] The Raman spectra of prepared samples further prove the XRD results, confirming the successful formation of prepared samples, which is in good agreement with previously reported work.[15a,33]

Further analysis was done on the prepared materials' porosity and surface area (Fig. 1d). The adsorption behavior of all samples exhibits type I isotherms, confirming that all prepared materials have microporous structures.[15a] The release of gas throughout the decomposition process of precursor materials or the IST process chemical reactions indicates the possible formation of hysteresis in the N_2-

isotherm. The prepared materials' surface area and porosity were determined using the amount of adsorbed N_2 at a temperature of −196 °C. The Brunauer–Emmett–Teller (BET) specific surface area of ZIF-8 and doped Fe and Ni@ZIF-8 are approximately 1718.62 $m^2\ g^{-1}$, 1439.92 $m^2\ g^{-1}$, and 1619.43 $m^2\ g^{-1}$, respectively, higher than the values reported in the literature.[15a,30] Also, the total pore volume values were recorded: 0.554 cc g^{-1}, 0.496 cc g^{-1}, and 0.521 cc g^{-1} for ZIF-8, Fe@ZIF-8, and Ni@ZIF-8, respectively (Table 1). ZIF-8 exhibits a higher specific surface area than doped ZIF-8. According to Fig. 1d, the doped Ni has little effect on the particular surface area, although Fe doping decreases the high surface area. The decline in surface area results from the presence of Fe and Ni particles on the surface and within the porous structure of the ZIF-8 materials. Using the IST method, the XRD and BET results confirm the absence of contaminants in the prepared materials. The characteristics of surface area and porosity for the as-prepared sample are presented in Table 1. The microstructure of the doped ZIF-8 was observed using TEM (Fig. 1e and f).

The crystal morphology of the prepared materials was further investigated using scanning electron microscopy analysis (SEM). The SEM images (Fig. 2a–c) reveal the presence of irregular particle morphologies with fused nanocrystals in the sample, possibly attributed to the short reaction time. As a result, rhombic dodecahedron crystals grew incompletely. The morphology of metal-doped ZIF-8 catalysts is seen as monodisperse nanoparticles with irregular particle morphologies with fused nanocrystal structure, suggesting that the presence of metal ions in the catalyst has minimal influence on the morphology of ZIF-8. Additionally, the lack of solvent in the IST system may lead to uneven material shapes, which agrees with the previously reported studies. For example, Lin *et al.* demonstrated the synthesis of MOF materials without using solvents or additives, resulting in a non-uniform distribution of particle sizes.[34] The TEM also confirmed the SEM. The elemental mapping of ZIF-8 and doped ZIF-8 was further confirmed using energy-dispersive X-ray spectroscopy (EDS) (Fig. S1–S3†). The analysis reveals the presence of five elements in the optimized hybrid, including oxygen (O), nitrogen (N), zinc (Zn), nickel (Ni), and iron (Fe). The corresponding images are illustrated in Fig. 2(d–f). The presence of all possible elements confirms the successful formation of materials.

ATR-FTIR was employed to identify the specific bonding groups of the synthesized materials. Due to the complexity of ZIF-8 material, it is difficult to identify each band in ZIF-8 and doped ZIF-8 FTIR spectra (Fig. S4†). Nevertheless, most bands are linked to the bonding within the imidazolate ring. The bands absorption below 800 cm^{-1} is attributed to the ring's out-of-plane bending, from 900 cm^{-1} to 1350 cm^{-1}, to the ring's in-plane bending; the entire ring stretching from 1300 cm^{-1} to 1500 cm^{-1}, at 1583 cm^{-1} for C═N stretching, and at 2930 and 3135 cm^{-1} for aliphatic and aromatic C–H stretching, respectively. Doped ZIF-8 samples exhibit the full ranges of bands in their FTIR spectra. However, slight changes can be seen in the bands corresponding to convoluted bands and C═N stretching. The FTIR spectra of ZIF-8 and doped ZIF-8 are consistent with the literature.[35]

X-ray photoelectron spectroscopy (XPS) determines the surface chemistry and valance states of ZIF-8 and dopped ZIFs (Fig. 3). The ZIF-8 and doped ZIF-8 are primarily composed of Zn 2p, C 1s, N 1s, Fe 2p, and Ni 2p, respectively. The spectra for ZIF-8, Fe@ZIF-8, and Ni@ZIF-8 are shown in Fig. 3(a). The high-resolution XPS spectra of Fe@ZIF-8, Ni@ZIF-8, and ZIF-8 are shown in Fig. 3(b–l), respectively. The deconvoluted profile of Zn 2p for both ZIF-8 and doped ZIF-8 is further classified into two bands consisting of $2p_{3/2}$ and $2p_{1/2}$. These bands are noticed at 1021.4 eV and 1044.5 eV, respectively, for all samples in which the presence of Zn(II) is confirmed (Fig. 3b, e, and i).[15a,36]

In Fig. 3c, the C 1s of the ZIF-8 displays a prominent C–C peak at 284.2 eV for the binding energy, in addition to shoulder peaks of C–O–C and O–C═C at 285.1 and 286.5 eV, respectively. Analogous C 1s peaks have been detected in doped ZIF-8. Fe@ZIF-8 displays a prominent C–C peak at 283.64 eV, with shoulder peaks denoting C–O–C and O–C═C at 284.24 and 285.11 eV, respectively (Fig. 3f). Ni@ZIF-8 shows the same peaks as Fe@ZIF-8 for C–C and C–O–C, while O–C═C at the binding energy of 284.83 eV is observed (Fig. 3j).[15a,36b,37] Fig. 3(d, g, and k) illustrate the N 1s ZIF-8 and doped ZIF-8 binding energy spectra. The presence of the imidazole ring in the prepared samples is confirmed by the deconvoluted peaks of N 1s ZIF-8, which are pyrrole-N, pyridine-N, oxidized-N, and graphitic-N.[15a] For ZIF-8, the Fe 2p and Ni 2p peaks are inconspicuous, confirming their absence in ZIF-8. The presence of Fe is confirmed by the deconvoluted profile of Fe 2p on Fe@ZIF-8 (Fig. 3h), which is further subdivided into $2p_{3/2}$ and $2p_{1/2}$ bands at 710.25 eV

Table 1 Surface area and porosity properties of the prepared sample

Sample	Surface area ($m^2\ g^{-1}$) BET	Langmuir	Pore size (nm)	Pore volume (cc g^{-1})	External surface area $m^2\ g^{-1}$	Product[a] (% yield)
ZIF-8	1003.705	1718.613	1.076	0.554	28.211	83
Fe@ZIF-8	870.206	1439.918	1.076	0.496	65.265	80
Ni@ZIF-8	932.808	1619.424	1.076	0.521	41.881	81

[a] The product yield was calculated from the average product weight acquired from two syntheses with theoretical molecular weight (MW) of ZIFs (ZIF-8 = 226 mol g^{-1}).

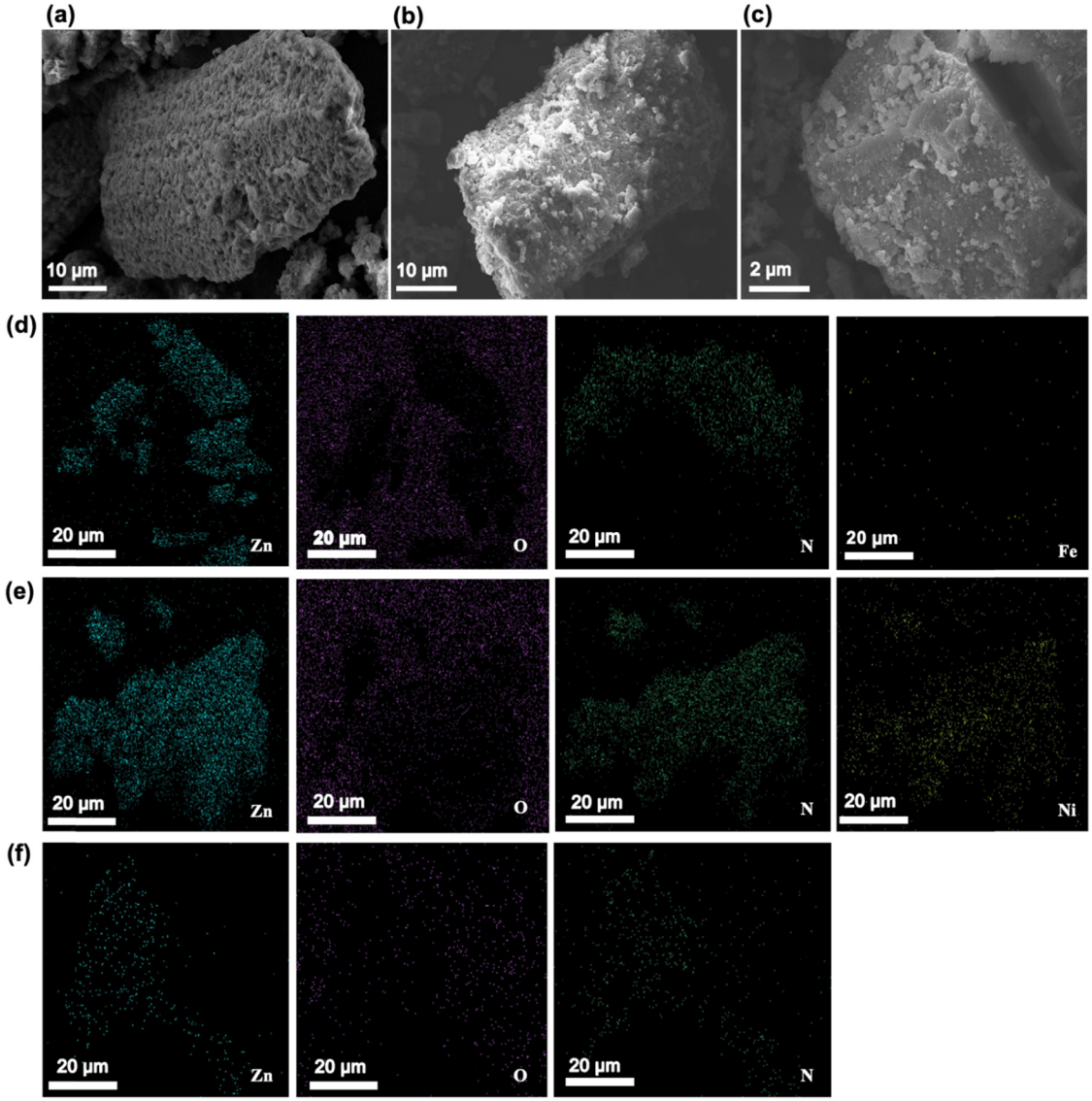

Fig. 2 SEM photos of (a) ZIF-8, (b) Fe@ZIF-8, and (c) Ni@ZIF-8, and FE-SEM images of the distributions of Zn, N, O, Ni, and Fe elements in (d) Fe@ZIF-8, (e) Ni@ZIF-8, and (f) ZIF-8.

and 723.96 eV, respectively.[38] Ni@ZIF-8 peak (Fig. 3l) at the binding energy of 854.1 eV and 871.7 eV is observed for Ni $2p_{3/2}$ and $2p_{1/2}$, respectively, confirming the presence of Ni doping.[39] The atomic percentage in the prepared sample calculated by XPS is shown in Table S1.† Therefore, the XPS measurements have confirmed the successfully synthesized ZIF-8 and doped ZIF-8.

As illustrated in Fig. S5,† UV-vis diffuse reflectance spectroscopy (DRS) was used to analyze the optical properties of the prepared photocatalyst. Fig. S5(a)† displays UV-vis spectra of the samples as they were prepared. ZIF-8's absorption spectrum shows a band span with a 340–390 nm wavelength interval. After incorporating Fe and Ni into ZIF-8, the UV-vis spectra display a UV absorption band similar to that of ZIF-8. Despite this, a slight variation in absorption margins is observed from 320 to 380 nm. The first band is attributed to the n–π* transition of the carbonyl group or the π–π* transition (–C═C–, sp^2 hybridization) and the trapped excited-state energy of surface states.[40]

The band gap energy has been calculated using UV-vis DRS analysis, as shown in Fig. S5(b).† The band gap energies of the prepared materials were calculated by plotting $(\alpha h\nu)^2$ *versus* photon energy ($h\nu$), where α represents the absorption coefficient. The energy band gaps are confirmed by the plot intercepts (dash lines) on the energy axis.[41] Fig. S5(b)† shows that the band gap value for ZIF-8 is 4.28 eV. In comparison, the band gap value (4.25 eV) of Fe@ZIF-8 is lower than ZIF-8. The band gap value of Ni@ZIF-8 is similar to that of ZIF-8. Notably, the band gap of ZIF-8 and doped ZIF-8 synthesized using the IST method is lower than in previously reported works.[2e,23,29a] The findings of this study indicate that ZIF-8 and doped ZIF-8 exhibit the ability to undergo photoexcitation, resulting in the generation of additional electron–hole pairs upon absorption of visible light. This

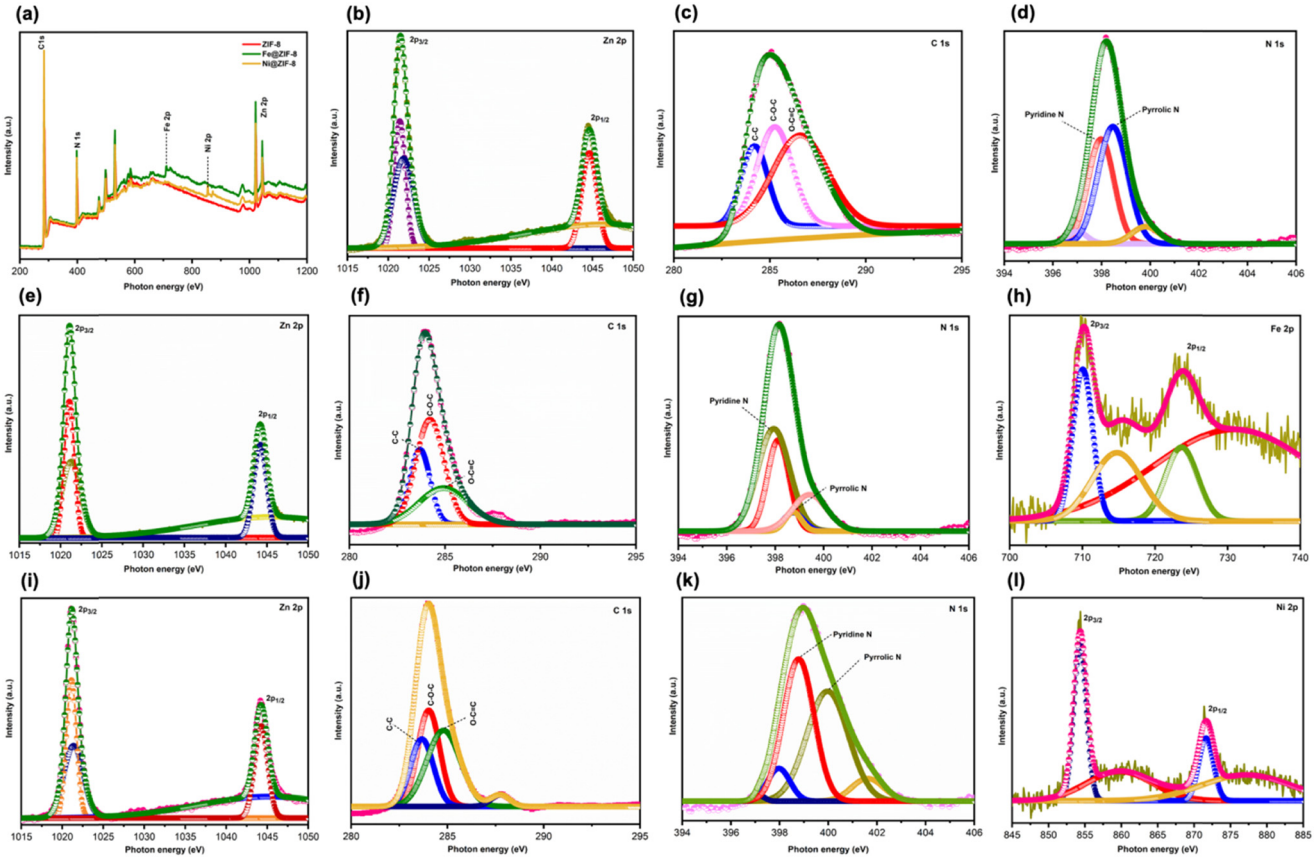

Fig. 3 XPS spectrum (a) XPS survey spectrum of ZIF-8, Fe@ZIF-8, and Ni@ZIF-8. High-resolution spectrum of ZIF-8, such as (b) Zn 2p, (c) C 1s, (d), N 1s, high-resolution spectrum of Fe@ZIF-8 such as (e) Zn 2p, (f) C 1s, (g) N 1s (h) Fe 2p, and high-resolution XPS spectrum of Ni@ZIF-8 such as (i) Zn 2p, (j) C 1s, (k) N 1s (l) Ni 2p, respectively.

phenomenon ultimately contributes to an enhanced photocatalytic efficiency.[41,42] Therefore, the observed morphological properties of the as-synthesized material are expected to adsorb and penetrate large dye molecules effectively.

3.2. Photocatalytic activity

3.2.1. Photocatalytic performance evaluation. To evaluate the photocatalytic efficiency of ZIF-8 and doped ZIF-8, we conducted a study using organic dyes, *i.e.*, MB and RhB, as a model photocatalytic reaction. We exposed the samples under visible-light illumination in static and dynamic systems. Before exposure to visible light, the dye solutions having the catalysis were kept in darkness for 30 minutes to establish the adsorption and desorption equilibrium, as seen in Fig. 4. In initial trial experiments, the absorption spectra of MB and RhB dyes were exposed to visible irradiations for 55–120 minutes. The results show that photolysis without catalysts caused less than a 1% degradation in the absorption spectra, revealing that the MB and RhB dye concentrations were the same.

As depicted in Fig. 4(a–c), the MB absorption spectra are reduced by employing the ZIF-8 and doped ZIF-8 under exposure to visible light for approximately 55 minutes. Under dark for 30 min, MB almost shows 7–38% adsorption using ZIF-8 and doped ZIF-8, respectively. The 94% degradation of MB with ZIF-8 is observed after applying the visible radiation exposure for around 55 minutes (Fig. 4a), while 7% absorption is observed under dark after 30 min. Using the Fe@ZIF-8 as a photocatalyst for the degradation of MB, almost 21% absorption happens in the dark after 30 min, and 99% of MB degrades under visible light after 55 min (Fig. 4b). In the case of Ni@ZIF-8, as shown in Fig. 4c, 38% absorption is observed after 30 min under dark, which is high compared to ZIF-8 and Fe@ZIF-8, while under visible light for 55 min, 95% MB photodegradation occurs. Fe@ZIF-8 is the most effective photocatalyst for MB degradation under visible light exposure compared to previous ZIF-8 and Ni@ZIF-8. All the prepared photocatalysts reveal good photocatalytic activity towards MB degradation under visible light during a short time compared to previously reported doped ZIF-8 prepared by executing conventional techniques.[2e]

The ZIF-8 and doped ZIF-8 photocatalytic activity was further examined for the degradation of RhB in the presence and absence of visible light irradiation (Fig. 4d–f). The prepared photocatalysts show different photocatalytic activity

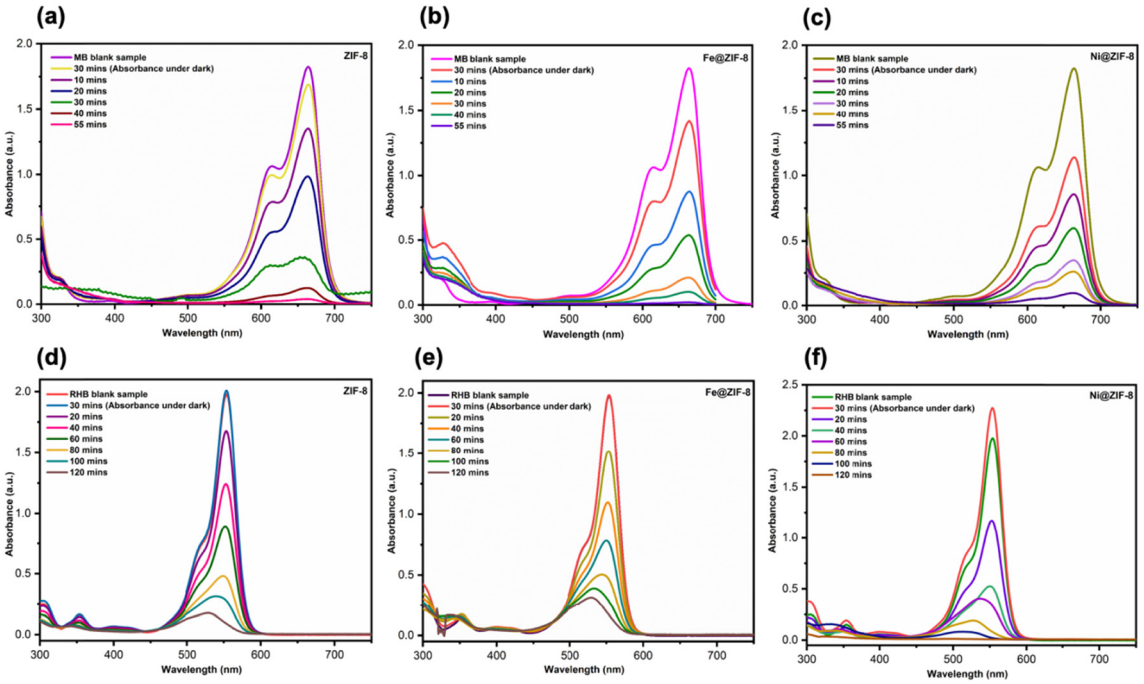

Fig. 4 UV-vis. Absorption change of MB in the presence of (a) ZIF-8, (b) Fe@ZIF-8, and (c) Ni@ZIF-8 under visible irradiation. UV-vis. Absorption change of RhB in the presence of (d) ZIF-8, (e) Fe@ZIF-8, and (f) Ni@ZIF-8 under visible irradiation.

towards the degradation of RhB compared to the photodegradation of MB. In the absence of visible light, ZIF-8 and Fe@ZIF-8 showed no absorbance of RhB under dark. In contrast, Ni@ZIF-8 shows an increment in the absorbance spectra of RhB under dark. The increase in absorbance of RhB using Ni@ZIF-8 is probably due to the desorption process and linked to the pH and surface charge of the semiconductor or photocatalyst,[43] as shown in Fig. 4f. Under the visible irradiation of about 120 min, the photodegradation of RhB for ZIF-8, Fe@ZIF-8, and Ni@ZIF-8 is 90.5%, 85.5%, and 99.5%, respectively. The best photocatalyst for degrading RhB under visible light is Ni@ZIF-8, which exhibits the complete degradation of RhB under visible light after 120 min. The Ni@ZIF-8 prepared *via* IST shows good photocatalytic activity towards the degradation of concentrated RhB compared to the recently reported doped Ru@ZIF-8 (ref. 15*a*) synthesized using solvothermal method in which photocatalytic activity was studied for 5 mg L^{-1} dye solution of RhB. The as-prepared photocatalyst shows a different trend toward the photodegradation of MB and RhB dyes. It is possibly due to the active site on the catalyst surface and metal, which are responsible for enhancing the degradation efficiency of the organic dyes.[15*a*]

Fig. S6(a and b)† display the MB and RhB degradation plots utilizing the ZIF-8 and doped ZIF-8 photocatalysts. The photodegradation efficiency curves indicate that Fe@ZIF-8 exhibits superior photocatalytic activity in the degradation of MB, surpassing both ZIF-8 and Ni@ZIF-8. By contrast, Ni@ZIF-8 shows remarkable photocatalytic activity in the degradation of RhB compared to ZIF-8 and Ni@ZIF-8. Interestingly, the differences in photocatalytic efficacy of the synthesized samples are insignificant in the case of MB.

The kinetic analysis provides significant details on the reaction pathways in the treatment process employing nanoparticles in an aqueous solution.[2*e*,44] Fig. S6(c and d)† illustrates the linear fitting plots of $\ln(C_0 - C_t) = K_{app\ t}$ for the as-prepared photocatalysts during the direct evaluations. The C_0 and C_t represent the starting and final concentrations of the MB and RhB dyes, respectively. The photodegradation of the MB and RhB using the as-prepared materials follows the pseudo-first-order kinetic models, with the squared correlation coefficient (R^2) of 0.96, 0.93, and 0.96 for the MB and 0.97, 0.99, and 0.89 for the RhB observed from their linear fitting plots (Fig. S6c and d†). The slope of the line fitting is denoted as the rate constant, k, in kinetics. Based on this study, the rate constant for the degradation of MB is 0.056, 0.070, and 0.048 min^{-1}, while the rate constants of RhB degradation are determined to be 0.02, 0.016, and 0.039 min^{-1}, respectively using ZIF-8, Fe@ZIF-8, and Ni@ZIF-8. As reported in the literature, the catalytic activity typically happens at the interface between the catalytic and dye materials.[15*a*,45] This is why a catalyst with a higher surface-to-volume ratio performs better in photocatalysis. During reduction and oxidation reactions, photocatalytic degradation occurs mainly on the catalyst's surface.[15*a*,45,46] Consequently, the active sites on the surface of photocatalysis become more accessible with the increment in the surface-to-volume ratio, resulting in a significant enhancement in the catalytic process. The outstanding Fe@ZIF-8 performance for MB and Ni@ZIF-8 for RhB can be attributed to their excellent surface-to-volume ratio when compared to the other catalysts.

3.2.2. The effects of dye's concentration and pH influence. The degradation rates under visible irradiation were also investigated to assess the MB concentration effect (10 and 20 mg L^{-1}) with the prepared photocatalysts. The 97% after 120 min, 95% after 75 min, and 99% after 90 min degradation of 20 mg L^{-1} MB under visible irradiations are observed using the ZIF-8, Fe@ZIF-8, and Ni@ZIF-8, as illustrated in Fig. 5a. The MB degradation rate using the as-prepared samples at the concentration of 10 mg L^{-1} is high (Fig. 4a–c), which is used to compare the degradation of MB with the concentration of 20 mg L^{-1}. The results suggest that the efficiency of MB decomposition is influenced by its commencing concentration, *i.e.*, the degradation rate decreases as the dye concentration increases. Accordingly, when the initial concentration of MB increases, the amount of dye adsorbed on the catalyst's surface also increases, leading to a decrease in the photocatalytic efficiency of the as-prepared materials. Furthermore, increasing dye concentration leads to a filter effect, which reduces the amount of incident irradiation used for dye excitation and consequently reduces the formation of reactive oxygen species (ROS).[15a,47]

Furthermore, the impact of the pH value in the dye solution is a considerable concern as it is linked to the properties of surface charge for the as-prepared photocatalysts during the reaction on its surface.[2e,48] The experiments were carried out at pH = 3 and 10 for MB using prepared photocatalysts under visible light irradiation, as displayed in the detailed results of Fig. 5(b and c). The absorbance spectra of the MB following 55 minutes of visible irradiations. In the presence of the prepared photocatalyst at pH 7 are shown in Fig. 4a–c. The inverse trend is found under pH = 10 along with the prepared photocatalyst, as seen in Fig. 5b. The 99% of MB dye removal is obtained using ZIF-8, Fe@ZIF-8, and Ni@ZIF-8 after 60, 35, and 45 minutes, respectively. Under the pH = 3, the MB degradation percentages are 95%, 97%, and 96% after 120, 80, and 90 min, respectively, in the presence of the prepared photocatalyst (Fig. 5c). Results show that pH = 7 and 11 enhances photocatalysis degradation of MB, leading to a more efficient and rapid generation of reactive oxygen species (ROS).[2e,48]

3.2.3. Recycling and stability of the photocatalyst. From a practical viewpoint, the long-term durability of the photocatalyst is a critical concern. The reusability and stability of the Fe@ZIF-8 photocatalyst in repeated MB degradation experiments have been investigated in photocatalytic analyses. The three cycles of catalytic reaction studies were performed under the same conditions with the as-prepared photocatalyst. Following every reaction, the photocatalyst was retrieved *via* centrifugation at 10000 rpm for five minutes, followed by rinsing with water and drying at 100 °C for eight hours before further processing. As shown in Fig. 6(a), the UV absorbance spectra of MB are similar in the first cycle under visible irradiations after 55 minutes of the initial experiment, which has been discussed in the photocatalytic performance section. A comparable pattern of photodegradation in MB is observed upon replicating the experiment for the second and third cycles; the outcomes are depicted in Fig. 6a. Notably, the as-prepared photocatalyst maintains its elevated photocatalytic activity even after three repetitions of the experiment, indicating that it can be effectively recycled. The percentage of the photocatalyst degradation during the three-time repetition experiment is illustrated in Fig. 6b. The MB photodegradation values in the presence of the Fe@ZIF-8 photocatalyst during the initial, second, and third cycles are 99%, 98%, and 93.5%, respectively. The decline in decolorization efficiency observed after the third repetition of the experiment can be attributed to catalyst loss during the rinsing and filtration processes. It is demonstrated that Fe@ZIF-8 can be reutilized effectively, suggesting that it functions as a stable and inexpensive catalyst when exposed to visible light. Eventually, the XRD and SEM analyses of Fe@ZIF-8 confirm that the morphology of Fe@ZIF-8 remains unchanged after three successive cycles, as seen in Fig. 6(c and d).

3.2.4. Photodegradation mechanism of MB. To get a more comprehensive picture of the MB's degradation processes with optimized Fe@ZIF-8 under visible light, we investigated the influence of reactive oxygen species (ROS) using a trapping species experiment. The degradation percentage of the MB in the presence of Fe@ZIF-8 photocatalyst using the

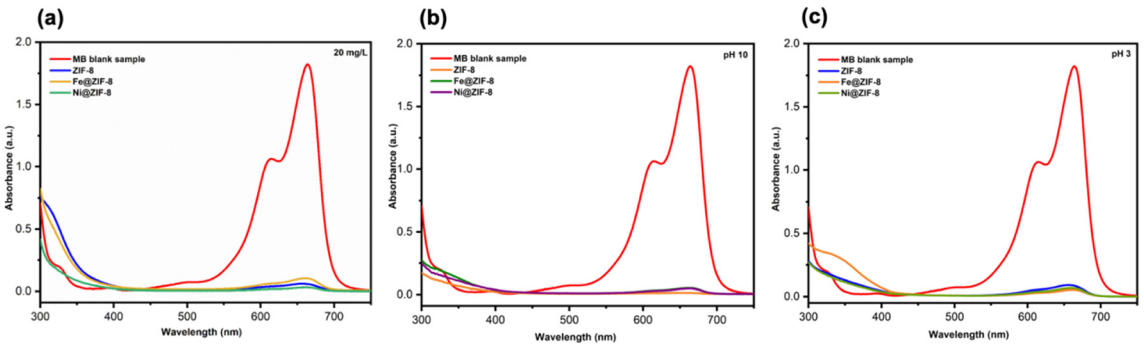

Fig. 5 (a) UV-vis. Absorption of 20 mg L^{-1} MB^{-1} using prepared samples and UV-vis. Absorption of MB using prepared samples under (b) pH 10 and (c) pH 3.

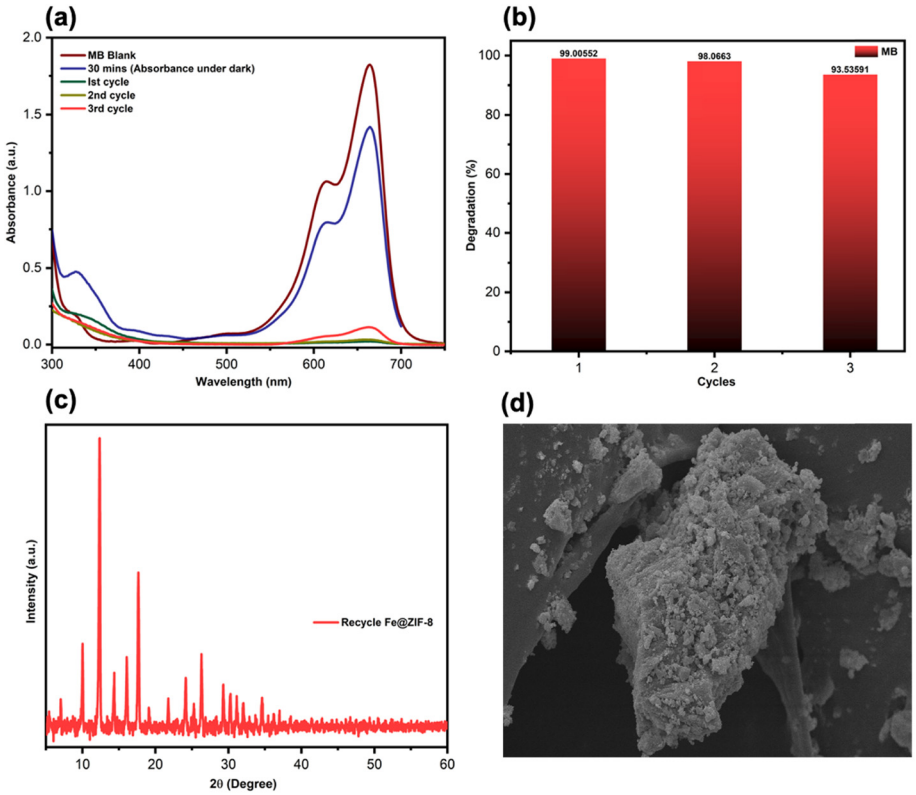

Fig. 6 (a) UV-vis. Absorption of MB and (b) MB photodegradation efficiency after 3rd cycle using Fe@ZIF-8, (c) X-ray diffraction pattern (XRD) after the 3rd cycle, (d) SEM of Fe@ZIF-8 after the 3rd cycle.

precise amounts of scavengers, *i.e.*, *p*-benzoquinone (BQ), isopropyl alcohol (IPA), and ammonium oxalate (AO), is provided in Fig. S8.† They are employed to identify the active hole (h^+), hydroxyl radical ($^{\bullet}OH$), and superoxide radical ($^{\bullet}O_2^-$) for the degradation of MB.[2e,15a,23] The active species comprising photogenerated h^+, $^{\bullet}OH$, $^{\bullet}O_2^-$, which significantly contributes to the MB photodegradation. The efficiency of the photocatalytic process is reduced by 26% and 30% with the addition of scavengers (BQ and AO), suggesting that both $^{\bullet}OH$ and $^{\bullet}O_2^-$ play a prominent role in the photodegradation of the MB dye. The photocatalytic activity decreases with the IPA as a scavenger, demonstrating the critical significance of the $^{\bullet}OH$ radical.[2e,23,49] Based on the abovementioned experimental results, Fig. 7 depicts the photodegradation pathway of MB dye under visible light in the presence of Fe@ZIF-8. According to eqn (3), when visible light photoexcited Fe@ZIF-8, the subjected light energy will be equal to or larger than its band gap energy, resulting in the formation of holes (h^+) and

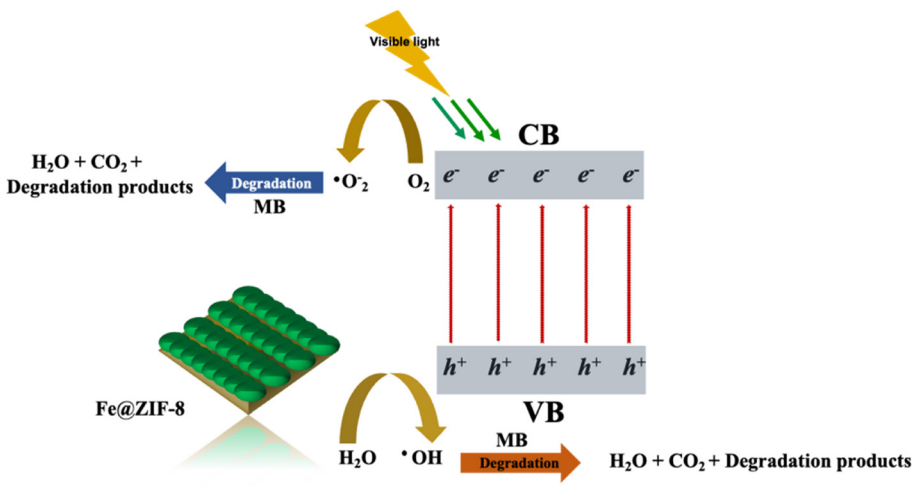

Fig. 7 Schematic illustration of the mechanism suggested for photocatalytic degradation of MB by Fe@ZIF-8.

electr3ons (e^-). The transfer of photogenerated electrons from Fe nanoparticles to ZIF-8 occurs due to the interactions between Fe nanoparticles and ZIF-8, which produces an electric field that spans several different energy band potentials. In the meantime, the movement of positive charges (h^+) from ZIF-8 to Fe nanoparticles co-occurs. Following the process, eqn (4) illustrates the formation of the ($^{\bullet}O_2^-$) *via* the photogenerated e^-. Furthermore, h^+ interacts with –OH and the adsorbed water to generate a hydroxyl radical ($^{\bullet}OH$), as seen in eqn (8) and (9). This radical then directly degrades the MB dye molecules, and the mechanism details are listed by eqn (3)–(11).

$$\text{Fe@ZIF-8} + h\nu \rightarrow \text{Fe@ZIF-8}\ (e^- + h^+) \quad (3)$$

$$e^- + O_2^- \rightarrow {}^{\bullet}O_2^- \quad (4)$$

$${}^{\bullet}O_2^- + H^+ \rightarrow {}^{\bullet}OOH \quad (5)$$

$${}^{\bullet}OOH + H^+ + e^- \rightarrow H_2O_2 \quad (6)$$

$$H_2O_2 + e^- \rightarrow {}^{\bullet}OOH + OH^- \quad (7)$$

$$h^+ + H_2O \rightarrow {}^{\bullet}OH + H^+ \quad (8)$$

$$h^+ + OH^- \rightarrow {}^{\bullet}OH \quad (9)$$

$$\text{MB} + \text{Visible light} \rightarrow [\text{MB}]^{\bullet} \quad (10)$$

$${}^{\bullet}OH + {}^{\bullet}O_2^- + [\text{MB}]^{\bullet} \rightarrow H_2O + CO_2 + \text{degradation products} \quad (11)$$

4. Conclusion

In summary, for the first time, we reported an *in situ* thermal (IST) approach for synthesizing high-porosity and crystalline doped ZIF-8 in good yield without solvents, additives, and post-treatment or an activation process in a short reaction duration. Moreover, the IST approach has been proven to be a cost-effective technique because it is free of the challenges of removing guest molecules from the final product. The photocatalytic efficiency of prepared materials using the IST method has been confirmed for the degradation of concentrated MB and RhB under visible light exposure. Based on the experimental outcomes, we demonstrate that under the optimum conditions, 98.4% and 99.5% degradation of MB and RhB are observed using Fe@ZIF-8 and Ni@ZIF-8 after 55 and 120 min, respectively. After three successive cycles, the optimized Fe@ZIF-8 shows good stability, recyclability, and almost 93.5% MB removal. A quenching experiment was used to investigate a plausible mechanism for MB in Fe@ZIF-8, and the scavenger experiment revealed that $^{\bullet}OH$ is the main radical for MB photolysis. The materials prepared using the IST method exhibit distinct advantages in chemical properties, giving rise to an improved photocatalytic performance.

Consequently, this IST method for synthesizing doped MOFs does not require hazardous reagents or solvents. Also, it can produce porous materials with a high yield within a short period. Therefore, this IST method allows for the development of highly efficient and stable environmentally friendly metal–organic frameworks for commercializing energy and environmental applications.

Data availability

Data available on request from the authors.

Author contributions

F. N. is responsible for conceptualization, methodology, experimentation, and original draft writing. C. H. M. is responsible for data curation. Z. W. is responsible for the experiment. H. T., S. P. S., M. D., J.-J. Kai, K.-C. C., C.-W. H., and W. N. are responsible for methods and validation. H.-Y. H. is responsible for supervision, funding acquisition, writing, and editing.

Conflicts of interest

The authors confirm that they have no known conflicting financial interests or personal ties that might have influenced the work presented in this study.

Acknowledgements

The authors acknowledge financial support from the Research Grants Council of Hong Kong (grant no. CityU 21203518 and F-CityU106/18), Innovation and Technology Commission (grant no. MHP/104/21), Shenzhen Science Technology and Innovation Commission (grant no. JCYJ20210324125612035, R-IND12303 and R-IND12304), City University of Hong Kong (grant no. 9229160, 9360140, 7005289, 7005580, 7005720, 9667213, 9667229, 9680331, 9052029 and 9678291), and National Natural Science Foundation of China (grant no. 51701159 and 21974131). Z. H thanks the National Key Research and Development Program of China (no. 2021YFA1500900) and the National Natural Science Foundation of China (no. 52071174).

References

1 (*a*) G. Karia, R. Christian and N. D. Jariwala, *Wastewater treatment: Concepts and design approach*, PHI Learning Pvt. Ltd., 2023; (*b*) C. A. Richard, Z. Pan, H.-Y. Hsu, S. Cekli, K. S. Schanze and J. R. Reynolds, *ACS Appl. Mater. Interfaces*, 2014, **6**, 5221–5227; (*c*) L. Fu, K. Fu, X. Gao, S. Dong, B. Zhang, S. Fu, H.-Y. Hsu and G. Zou, *Anal. Chem.*, 2021, **93**, 2160–2165; (*d*) X. Fu, T. He, S. Zhang, X. Lei, Y. Jiang, D. Wang, P. Sun, D. Zhao, H.-Y. Hsu and X. Li, *Chem*, 2021, **7**, 3131–3143; (*e*) H. Solayman, M. A. Hossen, A. Abd Aziz, N. Y. Yahya, K. H. Leong, L. C. Sim, M. U. Monir and K.-D. Zoh, *J. Environ. Chem. Eng.*, 2023, **11**, 109610.

2 (*a*) M. D. Khan, A. Singh, M. Z. Khan, S. Tabraiz and J. Sheikh, *J. Water Process Eng.*, 2023, **53**, 103579; (*b*) S. Rao, X. Zou, S. Wang, T. Shi, Y. Lu, L. Ji, H.-Y. Hsu, Q. Xu and X. Lu, *J. Electrochem. Soc.*, 2019, **166**, D427; (*c*) S. Javaid, X. Xu, W. Chen, J. Chen, H.-Y. Hsu, S. Wang, X. Yang, Y. Li, Z. Shao, F. Jones and G. Jia, *Nano Energy*, 2021, **89**, 106463; (*d*) S. P. Santoso, S.-P. Lin, T.-Y. Wang, Y. Ting, C.-W. Hsieh, R.-C. Yu, A. E. Angkawijaya, F. E. Soetaredjo, H.-Y. Hsu and K.-C. Cheng, *Int. J. Biol. Macromol.*, 2021, **175**, 526–534; (*e*) A. A. Abd El Khalk, M. A. Betiha, A. S. Mansour, M. G. Abd El Wahed and A. M. Al-Sabagh, *ACS Omega*, 2021, **6**, 26210–26220.

3 X. Dong, Y. Lin, G. Ren, Y. Ma and L. Zhao, *Colloids Surf., A*, 2021, **608**, 125578.

4 (*a*) M. Roy and R. Saha, *Intelligent environmental data monitoring for pollution management*, 2021, pp. 127–160; (*b*) H. Wu, T. H. Tan, R. Liu, H.-Y. Hsu and Y. H. Ng, *Solar RRL*, 2021, **5**, 2000423; (*c*) C.-N. Wu, L.-C. Sun, Y.-L. Chu, R.-C. Yu, C.-W. Hsieh, H.-Y. Hsu, F.-C. Hsu and K.-C. Cheng, *Food Chem.*, 2020, **330**, 127244; (*d*) M. S. Khan, Y. Li, D.-S. Li, J. Qiu, X. Xu and H. Y. Yang, *Nanoscale Adv.*, 2023, **5**, 6318–6348.

5 C. K. Benny and S. Chakraborty, *J. Environ. Manage.*, 2023, **331**, 117213.

6 (*a*) T. Xia, Y. Lin, W. Li and M. Ju, *Chin. Chem. Lett.*, 2021, **32**, 2975–2984; (*b*) X. Lei, M. You, F. Pan, M. Liu, P. Yang, D. Xia, Q. Li, Y. Wang and J. Fu, *Chin. Chem. Lett.*, 2019, **30**, 2216–2220; (*c*) H.-Y. Hsu, H.-H. Hsieh, H.-Y. Tuan and J.-L. Hwang, *Sol. Energy Mater. Sol. Cells*, 2010, **94**, 955–959; (*d*) X. Yang, J. Yang, M. I. Ullah, Y. Xia, G. Liang, S. Wang, J. Zhang, H.-Y. Hsu, H. Song and J. Tang, *ACS Appl. Mater. Interfaces*, 2020, **12**, 42217–42225; (*e*) A. Andreas, Z. G. Winata, S. P. Santoso, A. E. Angkawijaya, M. Yuliana, F. E. Soetaredjo, S. Ismadji, H.-Y. Hsu, A. W. Go and Y.-H. Ju, *J. Mol. Liq.*, 2021, **329**, 115579; (*f*) K. Tanji, I. El Mrabet, Y. Fahoul, I. Jellal, M. Benjelloun, M. Belghiti, M. El Hajam, Y. Naciri, A. El Gaidoumi and B. El Bali, *J. Water Process Eng.*, 2023, **53**, 103682.

7 A. Fujishima and K. Honda, *Nature*, 1972, **238**, 37–38.

8 C. Dong, J. Ji, Z. Yang, Y. Xiao, M. Xing and J. Zhang, *Chin. Chem. Lett.*, 2019, **30**, 853–862.

9 F. De Andrade, G. De Lima, R. Augusti, M. Coelho, J. Ardisson and O. Romero, *Chem. Eng. J.*, 2012, **180**, 25–31.

10 J. Miao, H. B. Lu, D. Habibi, M. H. Khiadani and L. C. Zhang, *Clean:Soil, Air, Water*, 2015, **43**, 1037–1043.

11 H. Liang, P. Hua, Y. Zhou, Z. Fu, J. Tang and J. Niu, *Chin. Chem. Lett.*, 2019, **30**, 2245–2248.

12 G. Li, X. Nie, Y. Gao and T. An, *Appl. Catal., B*, 2016, **180**, 726–732.

13 Y. Xue, Q. Chang, X. Hu, J. Cai and H. Yang, *J. Environ. Manage.*, 2020, **274**, 111184.

14 (*a*) F. Wang, J. Xu, Z. Wang, Y. Lou, C. Pan and Y. Zhu, *Appl. Catal., B*, 2022, **312**, 121438; (*b*) S. Rao, X. Zou, S. Wang, Y. Lu, T. Shi, H.-Y. Hsu, Q. Xu and X. Lu, *Mater. Chem. Phys.*, 2019, **232**, 6–15; (*c*) H.-Y. Hsu, L. Ji, C. Zhang, C. H. Mak, R. Liu, T. Wang, X. Zou, S.-Y. Leu and E. T. Yu, *J. Mater. Chem. C*, 2018, **6**, 11552–11560; (*d*) R. Liu, C. H. Mak, X. Han, Y. Tang, G. Jia, K.-C. Cheng, H. Qi, X. Zou, G. Zou and H.-Y. Hsu, *J. Mater. Chem. A*, 2020, **8**, 23803–23811; (*e*) F. Meng, Y. Jia, J. Wang, X. Huang, Z. Gui, L. Huang, R. Li, R. Chen, J. Xu, W. Chen, Z. He, H.-Y. Hsu, E. Zhu, G. Che and H.-L. Wang, *Solar RRL*, 2019, **3**, 1900319; (*f*) H. B. Truong, B. T. Huy, Y.-I. Lee, H. T. Nguyen, J. Cho and J. Hur, *Chem. Eng. J.*, 2023, **453**, 139777.

15 (*a*) I. Rabani, M. S. Tahir, F. Afzal, H. B. Truong, M. Kim and Y.-S. Seo, *J. Environ. Chem. Eng.*, 2023, **11**, 109235; (*b*) Z. Chen, H.-Y. Hsu, M. Arca and K. S. Schanze, *J. Phys. Chem. B*, 2015, **119**, 7198–7209; (*c*) H.-Y. Hsu, L. Ji, M. Du, J. Zhao, T. Y. Edward and A. J. Bard, *Electrochim. Acta*, 2016, **220**, 205–210; (*d*) C. H. Mak, X. Huang, R. Liu, Y. Tang, X. Han, L. Ji, X. Zou, G. Zou and H.-Y. Hsu, *Nano Energy*, 2020, **73**, 104752; (*e*) J. Abdi, *Colloids Surf., A*, 2020, **604**, 125330.

16 A. R. Millward and O. M. Yaghi, *J. Am. Chem. Soc.*, 2005, **127**, 17998–17999.

17 M. Jia, Y. Feng, S. Liu, J. Qiu and J. Yao, *J. Membr. Sci.*, 2017, **539**, 172–177.

18 P. Horcajada, T. Chalati, C. Serre, B. Gillet, C. Sebrie, T. Baati, J. F. Eubank, D. Heurtaux, P. Clayette and C. Kreuz, *Nat. Mater.*, 2010, **9**, 172–178.

19 L. E. Kreno, K. Leong, O. K. Farha, M. Allendorf, R. P. Van Duyne and J. T. Hupp, *Chem. Rev.*, 2012, **112**, 1105–1125.

20 (*a*) F. Naz, M. Ciprian, B. Mousavi, S. Chaemchuen, M. Zhu, S. Yan and F. Verpoort, *Eur. Polym. J.*, 2021, **142**, 110127; (*b*) C. H. Mak, R. Liu, X. Han, Y. Tang, X. Zou, H. H. Shen, Y. Meng, G. Zou and H. Y. Hsu, *Adv. Opt. Mater.*, 2020, **8**, 2001023; (*c*) C. H. Mak, X. Han, M. Du, J.-J. Kai, K. F. Tsang, G. Jia, K.-C. Cheng, H.-H. Shen and H.-Y. Hsu, *J. Mater. Chem. A*, 2021, **9**, 4454–4504; (*d*) Y. Peng, C. H. Mak, J.-J. Kai, M. Du, L. Ji, M. Yuan, X. Zou, H.-H. Shen, S. P. Santoso, J. C. Colmenares and H.-Y. Hsu, *J. Mater. Chem. A*, 2021, **9**, 26628–26649; (*e*) Y. Tang, C. H. Mak, R. Liu, Z. Wang, L. Ji, H. Song, C. Tan, F. Barrière and H. Y. Hsu, *Adv. Funct. Mater.*, 2020, 2006919; (*f*) F. Naz, M. Ciprian, Z. Luo, S. Yan, S. Z. Iqbal, M. Zhu, S. Chaemchuen and F. Verpoort, *Chem. Afr.*, 2021, 1–9.

21 (*a*) W. Pei, J. Zhang, H. Tong, M. Ding, F. Shi, R. Wang, Y. Huo and H. Li, *Appl. Catal., B*, 2021, **282**, 119575; (*b*) J. Qin, S. Wang and X. Wang, *Appl. Catal., B*, 2017, **209**, 476–482.

22 F. Naz, F. Mumtaz, S. Chaemchuen and F. Verpoort, *Catal. Lett.*, 2019, **149**, 2132–2141.

23 H.-P. Jing, C.-C. Wang, Y.-W. Zhang, P. Wang and R. Li, *RSC Adv.*, 2014, **4**, 54454–54462.

24 A. F. Gross, E. Sherman and J. J. Vajo, *Dalton Trans.*, 2012, **41**, 5458–5460.

25 Y.-R. Lee, J. Kim and W.-S. Ahn, *Korean J. Chem. Eng.*, 2013, **30**, 1667–1680.

26 (*a*) Y.-R. Lee, M.-S. Jang, H.-Y. Cho, H.-J. Kwon, S. Kim and W.-S. Ahn, *Chem. Eng. J.*, 2015, **271**, 276–280; (*b*) F. Lorignon, A. Gossard and M. Carboni, *Chem. Eng. J.*, 2020, **393**, 124765; (*c*) Y. Tang, C. H. Mak, G. Jia, K.-C. Cheng, J.-J. Kai, C.-W. Hsieh, F. Meng, W. Niu, F.-F. Li, H.-H. Shen, X. Zhu, H. M. Chen and H.-Y. Hsu, *J. Mater. Chem. A*, 2022, **10**,

12296–12316; (*d*) Y. Tang, C. H. Mak, J. Zhang, G. Jia, K.-C. Cheng, H. Song, M. Yuan, S. Zhao, J.-J. Kai, J. C. Colmenares and H.-Y. Hsu, *Adv. Mater.*, 2023, **35**, 2207835; (*e*) C. H. Mak, Y. Peng, M. H. Chong, L. Yu, M. Du, L. Ji, X. Zou, G. Zou, H.-H. Shen and S. P. Santoso, *J. Mater. Chem. C*, 2023, **11**, 11303–11311; (*f*) Y. Tang, C. H. Mak, C. Wang, Y. Fu, F.-F. Li, G. Jia, C.-W. Hsieh, H.-H. Shen, J. C. Colmenares, H. Song, M. Yuan, Y. Chen and H.-Y. Hsu, *Small Methods*, 2022, **6**, 2200326; (*g*) J. Wang, S. Chaemchuen, N. Klomkliang and F. Verpoort, *Cryst. Growth Des.*, 2021, **21**, 5349–5359.

27 M. Dahl, Y. Liu and Y. Yin, *Chem. Rev.*, 2014, **114**, 9853–9889.

28 J. Wang, L. Yuan, P. Zhang, J. Mao, J. Fan and X. L. Zhang, *Nanoscale*, 2024, 7323–7340.

29 (*a*) K. Li, N. Miwornunyuie, L. Chen, H. Jingyu, P. S. Amaniampong, D. Ato Koomson, D. Ewusi-Mensah, W. Xue, G. Li and H. Lu, *Sustainability*, 2021, **13**, 984; (*b*) Y. Zhou, Y. Wang, Z. Chen, H. Gong, L. Chen and H. Yu, *J. Phys. Chem. C*, 2023, **127**, 7184–7196; (*c*) O. Assila, N. Vilaça, A. R. Bertão, A. M. Fonseca, P. Parpot, O. S. Soares, M. F. Pereira, F. Baltazar, M. Bañobre-López and I. C. Neves, *Chemosphere*, 2023, **339**, 139634; (*d*) Z. M. Lighvan, S. R. Hosseini, S. Norouzbahari, B. Sadatnia and A. Ghadimi, *Fuel*, 2023, **351**, 128991; (*e*) A. Paul, I. K. Banga, S. Muthukumar and S. Prasad, *ACS Omega*, 2022, **7**, 26993–27003; (*f*) E. M. Khudhair, Y. S. Kareem, S. H. Ammar and A. S. Mahdi, *Mater. Today: Proc.*, 2023, DOI: **10.1016/j.matpr.2023.04.058**.

30 L. Hu, L. Chen, X. Peng, J. Zhang, X. Mo, Y. Liu and Z. Yan, *Microporous Mesoporous Mater.*, 2020, **299**, 110123.

31 B. Wang, A. P. Côté, H. Furukawa, M. O'Keeffe and O. M. Yaghi, *Nature*, 2008, **453**, 207–211.

32 F. Adar, *Spectroscopy*, 2014, 29.

33 G. Kumari, K. Jayaramulu, T. K. Maji and C. Narayana, *J. Phys. Chem. A*, 2013, **117**, 11006–11012.

34 J.-B. Lin, R.-B. Lin, X.-N. Cheng, J.-P. Zhang and X.-M. Chen, *Chem. Commun.*, 2011, **47**, 9185–9187.

35 (*a*) S. Sharma, K. Sudarshan, A. Yadav, S. Jha, D. Bhattacharyya and P. Pujari, *J. Phys. Chem. C*, 2019, **123**, 22273–22280; (*b*) S. Bhattacharyya, S. H. Pang, M. R. Dutzer, R. P. Lively, K. S. Walton, D. S. Sholl and S. Nair, *J. Phys. Chem. C*, 2016, **120**, 27221–27229.

36 (*a*) M. T. Thanh, T. V. Thien, P. D. Du, N. P. Hung and D. Q. Khieu, *J. Porous Mater.*, 2018, **25**, 857–869; (*b*) B. Shen, B. Wang, L. Zhu and L. Jiang, *Nanomaterials*, 2020, **10**, 1636.

37 S.-W. Lv, J.-M. Liu, N. Zhao, C.-Y. Li, Z.-H. Wang and S. Wang, *New J. Chem.*, 2020, **44**, 1245–1252.

38 P. Liu, S. Liu and S.-W. Bian, *J. Mater. Sci.*, 2017, **52**, 12121–12130.

39 Z. Fu, J. Hu, W. Hu, S. Yang and Y. Luo, *Appl. Surf. Sci.*, 2018, **441**, 1048–1056.

40 J. Ju and W. Chen, *Biosens. Bioelectron.*, 2014, **58**, 219–225.

41 S. Goyal, M. S. Shaharun, C. F. Kait and B. Abdullah, *J. Phys.: Conf. Ser.*, 2018, **1123**, 012062.

42 V. Jeyalakshmi, R. Mahalakshmy, K. Krishnamurthy and B. Viswanathan, *Indian J. Chem.*, 2012, 1263–1283.

43 H. Mallah, D. Naoufal, A. Safa and M. El-Jamal, *Port. Electrochim. Acta*, 2013, **31**, 185–193.

44 É. C. Lima, M. A. Adebayo and F. M. Machado, *Carbon nanomaterials as adsorbents for environmental and biological applications*, 2015, pp. 33–69.

45 S. Dey, S. Das and A. K. Kar, *Mater. Chem. Phys.*, 2021, **270**, 124872.

46 Q. Wan, T. Wang and J. Zhao, *Appl. Phys. Lett.*, 2005, 87.

47 (*a*) M. Shaban, A. M. Ahmed, N. Shehata, M. A. Betiha and A. M. Rabie, *J. Colloid Interface Sci.*, 2019, **555**, 31–41; (*b*) L. Yang, L. Xu, X. Bai and P. Jin, *J. Hazard. Mater.*, 2019, **365**, 107–117.

48 M. F. Hanafi and N. Sapawe, *Mater. Today: Proc.*, 2020, **31**, 272–274.

49 T. V. Tran, M. Alsaiari, F. A. Harraz, W. Nabgan, D. T. D. Nguyen and C. V. Nguyen, *Water*, 2023, **15**, 2186.